applied optics

Waveguide based passively demodulated photothermal interferometer for light absorption measurements of trace substances

BRADLEY VISSER,[1,2] JONAS BILAL,[1] NIKOLAUS FLÖRY,[3] MANUELA WIPF,[1] PETER STEIGMEIER,[1] TOBIAS RÜGGEBERG,[1] FELIX BETSCHON,[3] AND ERNEST WEINGARTNER[1,*]

[1]Institute for Sensors and Electronics, University of Applied Sciences and Arts Northwestern Switzerland, CH-5210 Windisch, Switzerland
[2]Current address: Mems AG, CH-5413 Birmenstorf, Switzerland
[3]vario-optics AG, CH-9410 Heiden, Switzerland
*Corresponding author: ernest.weingartner@fhnw.ch

Received 30 September 2022; revised 21 November 2022; accepted 22 November 2022; posted 23 November 2022; published 4 January 2023

In this contribution, we present the development of a passively demodulated interferometer based on 3 × 3 waveguide couplers to measure light absorption of trace gases and aerosol particles via the photothermal effect. In contrast to a "classical" interferometer with two outputs, active quadrature control is not required to ensure a high sensitivity of the system. An algorithm for the evaluation of the photothermal interferometry signal from the outputs of asymmetric 3 × 3 couplers is detailed. The performance of the algorithm is demonstrated with NO_2 calibration experiments using couplers with different working principles (i.e., fused-fiber and planar-waveguide based). The results of a laboratory measurement campaign using aerosolized nigrosin are discussed, and the measured aerosol absorption is compared to a reference instrument. A noise analysis shows interferometer phase noise to be the primary noise component. Improvements to the setup are recommended, which should improve the current instrumental detection limit in terms of absorption coefficient to below the current value of 100 Mm^{-1} (1σ, 60 s). This corresponds to mass concentrations of about 10 $\mu g/m^3$ for submicrometer-size black carbon particles.

https://doi.org/10.1364/AO.476868

1. INTRODUCTION

The motivation for the development presented here is the need to develop smaller and more cost-effective devices to monitor air quality. Particular attention has been paid to the carbonaceous particles produced by incomplete combustion of fossil fuels and biomass, e.g., in transportation, home heating, and forest fires. They have recently attracted the attention of the scientific community and policymakers [1]. In particular, black carbon (BC), a specific component of aerosols produced in combustion processes, is considered a serious risk to human health [2]. Additionally, BC particles are efficient light absorbers, with light absorption leading to local heating of the environment and thus contributing significantly to global warming [3,4].

Online determination of BC particle concentrations typically uses light absorption measurements in the visible and near-infrared spectral regions [5]. Absorption measurements are selective as only specific particles absorb light at these wavelengths, namely, predominantly BC and other carbonaceous aerosols. However, reference absorption instruments used in monitoring networks are both expensive and bulky, limiting their deployment to representative locations. For the reduction of BC exposure, it is important to be able to reliably measure BC concentrations in urban areas with dense measurement networks to identify the emitting sources.

In this contribution, we report on the initial development of a light absorption sensor based on photothermal interferometry (PTI), with the intention of developing a portable device to measure BC concentrations by utilizing waveguide technology. This new technology is interesting because it is more stable and easier to adjust than free-space systems. It has the potential to pave the way for smaller, more portable, and cheaper environmental sensors.

A. Photothermal Interferometry

Photothermal interferometry is a technique in which the light absorption of a sample is determined via the differential change of the optical path length in an interferometer. A modulated pump beam intersects one beam path of the interferometer. Absorption of pump beam light in the sample causes a local temperature increase. As the refractive index of a gas depends upon its temperature, a modulation of the refractive index (optical path length) results, and modulation of the phase is produced in the interferometric sensor. In a homodyne measurement, the induced phase modulation is observed as a modulation of the light intensity at the interferometer outputs.

PTI has been commonly employed for measurements of light absorption by gases [6–8], but also aerosol particles [5,9–17]. While there are some examples of PTI gas sensors employing optical glass fibers [16,18], previous realizations of PTI instruments for aerosol light absorption measurements have been large, laboratory-based devices based on free-space laser beams. However, PTI has a unique potential for miniaturization, as the sensitive measurement volume can be made almost indefinitely small—it is defined by the overlap of the pump and probe lasers.

Apart from glass fiber technology, the emerging field of photonic integrated circuits (PICs) exhibits tremendous potential for the miniaturization of optical sensors. Interferometric schemes benefit from the reduction in size (entire interferometers can be built on a centimeter-sized chip), as well as from increased stability, due to the elimination of vibration-prone free-space elements. Additionally, PIC technology enables the design of photonic components, which are either not available or difficult to realize in free space. One such component are $N \times N$ couplers, where $N > 2$. Employing such couplers as the beam-recombination optics in interferometers prevents the complete phase-dependent signal fading that is characteristic of standard two-output interferometers.

The prevention of signal fading is exceedingly important for PTI measurements, given that the PTI signals for typical ambient concentrations of BC are ≪1 mrad. By employing an $N \times N$ coupler as beam-recombining optic, phase quadrature control (regulation to the most sensitive operating point) is no longer required, which reduces the hardware requirements of the system. Instead of a 180° phase shift as in a standard two-output interferometer, a symmetric 3×3 coupler results in three output signals that are ideally phase shifted by 120° with respect to one another. In order to reconstruct the PTI signal, an advanced algorithm is required to process the signals, taking into account the phase dependence of the individual signals and compensating for the phase dependence of the total sensitivity.

The use of 3×3 couplers in the demodulation of interferometric signals was introduced in the early 1980s [19–21]. Many algorithms [22–31] are available for demodulating phase shifts. They make the basic assumption of a symmetric 3×3 coupler with phase differences between the individual outputs of exactly 120° and equal amplitudes and offsets. However, in real devices, the phase differences and signal contrasts can deviate significantly from this symmetric case, and more sophisticated algorithms [26,32–34] are necessary to recover the phase information of the system.

In this contribution, we present a compact yet powerful waveguide PTI sensor scheme for the measurement of aerosol light absorption and propose a new algorithm for the evaluation of the PTI signal. It features a small footprint sensor system, which makes use of fiber- and integrated-photonic technologies. Furthermore, a novel, general-use algorithm is presented, which allows us to retrieve the PTI signal from asymmetric 3×3 interferometric combiners. The usability of the algorithm is demonstrated with initial measurement results using two different 3×3 couplers with different working principles (fused-fiber and planar-waveguide based), including a calibration using NO_2 and the response of the sensor to varying concentrations of light-absorbing carbonaceous aerosols. Finally, a noise attribution is discussed, from which the current limitations of the sensor can be drawn, and strategies for improvement are presented.

2. THEORY ON PHOTOTHERMAL INTERFEROMETRY

The theory of the photothermal effect is covered in detail in the publications of Sedlacek and Moosmüller [13–15] and is only presented here in brief. Light absorption in the sample leads to a temperature increase of the absorbing species, and this heat is transferred to the surrounding gas via conduction. The temperature increase of the gas leads to a change of the real part of the local refractive index, which is approximated by

$$\Delta n = \frac{n-1}{T_0} \Delta T, \tag{1}$$

where n is the refractive index of the gas at its initial temperature T_0. For a measurement made using a modulated light source, henceforth the pump beam, inside one arm of an interferometer, the initial increase of the refractive index Δn causes a phase shift $\Delta\varphi$ of a light wave passing through this region with respect to a reference light wave, which is directly proportional to the light absorption coefficient (b_{abs}) of the sample [15]:

$$\Delta\varphi = \frac{2\pi \cdot (n-1)}{\lambda_{probe} \cdot T_0 \cdot \rho \cdot C_p} \cdot \frac{l \cdot P_{Pump}}{A} \cdot b_{abs} \cdot \Delta t. \tag{2}$$

The first factor can be considered as a constant, where λ_{probe} is the wavelength of the probe laser; ρ and C_p are the density and heat capacity of the gas, respectively. The second factor determines the sensitivity of the instrument and is given by the power of the pump beam P_{Pump} and the geometrical beam arrangement: l and A are the length and cross-sectional area of overlap of the pump and probe beams. The pump beam is modulated, and care must be taken to ensure that the duration of the laser high phase Δt is sufficiently short to avoid temperature saturation effects and to remain within the linear response range.

By calibrating the response of the interferometer to a gas of known absorption, Eq. (2) can be reduced to

$$b_{abs} = C \cdot \Delta\varphi, \tag{3}$$

where C is the calibration factor obtained from the calibration measurement. For the case of a traditional two-output interferometer (with equal output intensities and high contrasts) actively held in phase quadrature and $\Delta\varphi \ll 1$ rad, the phase modulation caused by the PTI effect can easily be determined from the measured intensity change at the outputs:

$$\Delta\varphi \cong \frac{1}{2} \left| \frac{I_{1,f} - I_{2,f}}{I_1 + I_2} \right|, \tag{4}$$

where I_n represents the measured intensity at output n, and subscript f is the evaluation of the measured signal at the pump laser modulation frequency.

In this work, the evaluation of a PTI signal $\Delta\varphi$ will be extended to the case of a passively demodulated system without quadrature control and three (asymmetric) outputs.

3. EXPERIMENTAL PTI SETUP AND DATA ACQUISITION

In this subsection, we present the physical design of our newly developed waveguide-based PTI, which we have named MiniPTI.

A. Realized Waveguide-Based PTI

The MiniPTI is realised in the form of a Mach–Zehnder interferometer. A 1×2 coupler is used to split the incoming laser beam into two probe beams (reference and measurement) as schematically depicted in Fig. 1. After the 1×2 coupler, the probe beams are free-space coupled using gradient-index (GRIN) lenses. The collimated beams then enter two chambers, where a second laser (pump beam) is used to induce the photothermal effect. Both probe beams are coupled back into the waveguide and recombined in the 3×3 coupler. Light intensity at each output is monitored using a photodiode.

Two different probe lasers were used in the experiments: (a) a pig-tailed single-frequency distributed feedback (DFB) solid-state laser from Thorlabs operating at 1310 nm with an optical power of 2 mW (LP1310-SAD2) and (b) a pig-tailed single-frequency DFB solid-state laser from DK Photonics (FL-1310-20-SM-B) with an optical power of 20 mW. All optical fibers are of the type SMF-28. The laser pigtail is directly connected to the input of a fused-fiber 1×2 coupler ([35], product ID 65798), which divides the amplitude of the incoming light 50:50 between the two outputs. The outputs are connected to a pair of pig-tailed GRIN lenses ([35], product ID 123939, working distance: 20 mm) that are mounted in the chambers (see below for more details). Light exits the GRIN lenses, traverses the chamber, and is collected by a second pair of GRIN lenses. The pigtails of the GRIN lenses are connected directly to two inputs of a 3×3 coupler (either a fused-fiber coupler or a planar waveguide device; see below).

The setup is custom-built out of stainless steel and consists of two individual chambers, which are denoted the measurement and reference chambers. The two chambers are separated by a glass window, with two further windows mounted at either end of the chamber to allow the passage of the pump laser. The GRIN lenses are mounted in custom four-axis adjustable mounts, which can be fixed via setscrews following adjustment. Flanges are mounted to the tops of the two chambers that allow visual alignment of the pump and probe beams once removed. The pump laser is a Fabry–Perot type laser diode operating at 450 nm, which was used at a power of 1 W (Thorlabs, L450P1600MM). The laser diode is mounted in a temperature-controlled mount, and the pump laser is amplitude modulated at the desired measurement frequency ($f_{\mathrm{mod}} < 200$ Hz, typically 80 Hz). The beam is focused into the aerosol chamber using a spherical singlet lens and is adjusted to coincide with the probe beam in the measurement chamber. The high pump laser power was necessary to achieve sufficient sensitivity to measure environmentally relevant concentrations of trace substances. A lower excitation power could be employed if noise sources or beam overlap can be improved in a future setup.

B. Passive Phase Demodulation Using Waveguide Couplers

The realization of a PTI without quadrature control requires that the sensitivity of the measurement does not go to zero at any interferometric phase. This is not possible for a standard two-output interferometer with a phase difference of 180° between the outputs, whereby the sensitivity of the measurement goes to 0 for interferometric phases of $\frac{n}{2}360°$ ($n = 0, \pm1, 2, 3, \ldots$). To overcome this, a different phase relation between the outputs is required. Waveguide-based $N \times N$ couplers ($N \geq 3$) provide a practical solution to increase the number of outputs, and thus an opportune phase relation, compared to what is easily achievable in a free-space system.

In order to demonstrate the extended usability of the developed signal analysis algorithm (described below), experiments have been performed with two 3×3 couplers of different working principles and different characteristics. First, we used

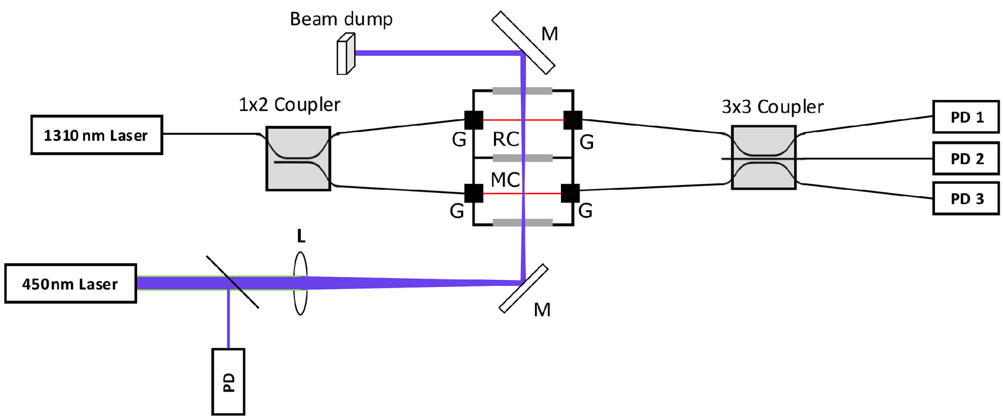

Fig. 1. Schematic of the waveguide-based photothermal interferometer with a fiber-coupled probe laser (1310 nm) and a free-space pump laser (450 nm). The 1×2 coupler generates two probe beams, which are collimated with GRIN lenses (G) into the measurement chamber (MC) and reference chamber (RC). These beams are recombined with a 3×3 coupler, and the light absorption of the pump laser in the measurement chamber is retrieved from the three measured intensities (PD 1, PD 2, PD 3). A lens (L) and mirrors (M) are used to focus the pump beam into the probe beam in the measurement chamber.

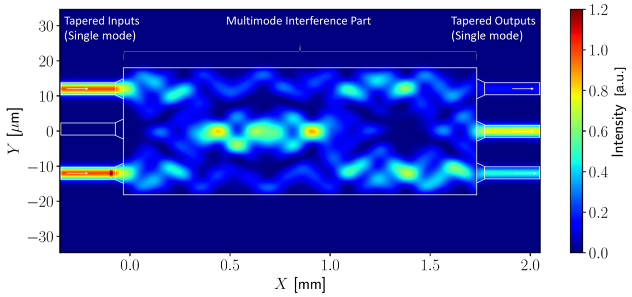

Fig. 2. Working principle of the multimode interference coupler (MMI). The colors show the intensity distribution of the modeled interference pattern when light with a phase shift of 22.3° is injected at the two outer inputs on the left. The center input is not used in the experiments. Note that dimensions are not to scale: the horizontal dimension (X) is in millimeters (mm), and vertical one (Y) is in micrometers (μm).

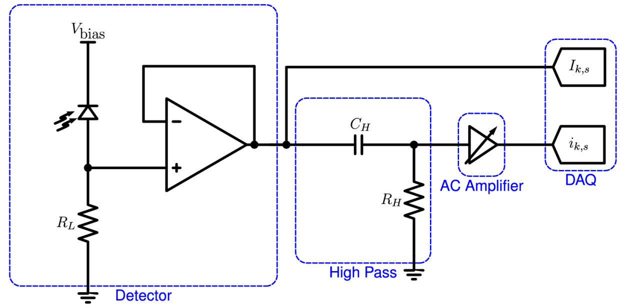

Fig. 3. Schematic electronic circuit for obtaining the DC ($I_{k,s}$) and AC ($i_{k,s}$) signals. The AC amplifier has an adjustable gain with possible values of 10, 100, and 1000.

a fused-fiber coupler ([35], product ID 65798) made by fusing three fibers to distribute the input power of any one fiber equally among the three output fibers. Any incoming beam is ideally split between the three outputs in the ratio 1/3:1/3:1/3. Used in an interferometer, phase differences of 120° between the three respective outputs are ideally obtained.

The other 3 × 3 coupler investigated was custom designed at [36] based on their integrated planar waveguide technology [37]. In this platform, photonics devices are defined photolithographically using optical polymer materials. In contrast to the fused-fiber coupler, the planar waveguide device is based on a multimode interference (MMI) coupler. This photonic structure consists of a wide multimode waveguide body, accessed by single-mode waveguide input ports and terminated by a number of single-mode output ports (see Fig. 2). The number of input and output ports can be freely chosen, so in principle, any coupler configuration of the form $N \times M$ (where $N \leq M$) can be realized. The actual length of the MMI-based 3 × 3 coupler is only 2 mm (as compared to the centimeter-size fused-fiber coupler). This demonstrates a path toward further miniaturization, enabling a complete PTI scheme directly on a photonic chip. In order to connect the MMI chip to the aerosol chamber, a waveguide fan-out and fiber pigtails were used. The fiber pigtails increase the interferometric path lengths, i.e., the length of the fibers that lie between the first (1 × 2 splitter) and the second (3 × 3 combiner) coupler. This length is important because even the smallest vibrations or temperature fluctuations can cause disturbances in these paths. Based on the selection of available components, the path length was 76 cm when using the fused-fiber coupler as the second coupler. With the MMI coupler, the path length changes to 84 cm.

C. Analog Signal Processing and Data Acquisition

The beams exiting each of the three outputs impinge on three separate photodetectors PD (FC/PC-coupled photodetector) which each contain a photodiode (Thorlabs, FGA01–InGaAs). For the signal conditioning, the photodiodes are connected directly to custom-built electronics (see Fig. 3).

The circuitry is designed to provide DC- and AC-coupled signals from each photodetector to the data acquisition unit (DAQ). The photocurrents from the photodiodes are converted to voltages using a load resistor R_L and fed into a voltage buffer. The resistor R_L is chosen so that the DC-coupled signals $I_{k,s}$ are trimmed to be close to the full-scale rail of the DAQ. The index $k = 1, 2, 3$ in $I_{k,s}$ denotes the channel number, and the subscript s the sample index. In parallel, the photodetector signals are high pass filtered via a first order high pass with a cutoff frequency of 34 Hz to obtain AC-coupled signals $i_{k,s}$. The AC signals are subsequently amplified by up to 3 orders of magnitude using a non-inverting instrumentation amplifier to optimally use the full range of the DAQ and increase the resolution of these small signals. The DAQ (National Instruments, USB-6356) is operated with a sampling frequency of 50 kHz and is connected via USB to a PC running a custom LabVIEW program, which generates a (hardware buffered) reference square-wave signal for the modulation of the pump laser. The incoming DC- and AC-coupled signals are digitized with 16-bit resolution and stored together with the modulation signal.

A separately executed Python script processes these measured values, and the DC signals are then used to calculate the current phase of the interferometer. Lock-in amplification is applied to the digitized AC-coupled signals, using the signal from a photodiode observing a reflection of the pump laser (see Fig. 1) as the seed for the generation of a sinusoidal reference signal. PTI signal retrieval algorithms (introduced in the following section) are then employed on the lock-in filtered signals.

4. SIGNAL ANALYSIS AND RETRIEVAL OF PTI SIGNAL

This section describes how the measured PD signals are processed to obtain the interferometric phase and the PTI signal. Figure 4 schematically shows the three detector signals as a function of the phase φ of the interferometer. In this example, the three detector signals are phase-shifted by 120° and have different contrasts, which are expressed in different minimum and maximum values. Such data is experimentally obtained by performing a phase scan, during which the optical path length in one arm is changed by changing the pressure in one of the chambers. In normal operation, the interferometer phase φ is not regulated to a specific value and is subject to random drifts

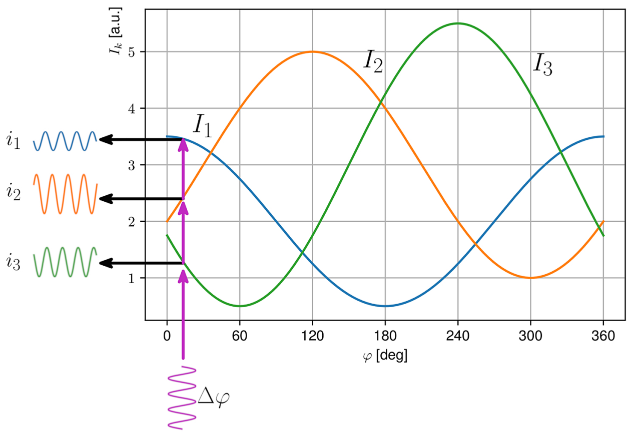

Fig. 4. Measured DC signals I_k and AC signals i_k with respect to the current interferometric phase φ. The PTI effect induces a modulation of the interferometric phase $\Delta\varphi$, which is recorded as lock-in-demodulated signals i_k, whose amplitudes and phases depend on the derivatives of the respective DC curves.

caused, for example, by changes in the pressure or temperature differences between the two chambers. The modulation of the pump laser at a fixed frequency (typically 80 Hz) causes a small periodic phase change $\Delta\varphi$ as described in Eq. (2). The figure shows an example of the relationship between PTI-induced phase modulation ($\Delta\varphi$) and the observed intensity demodulation (i_k) at an arbitrarily chosen phase. The derivative of the intensity I_k at the prevailing interferometric phase determines the measured AC coupled amplitude. Note that a phase shift of 180° is introduced on the demodulated signals when the derivative of the sine changes from positive to negative.

After digitization, the DC and demodulated AC signals are processed in order to retrieve the PTI signal $\Delta\varphi$ according to the signal flow diagram presented in Fig. 5.

All input signals are acquired at a sampling frequency much higher than the modulation frequency to ensure a clean reproduction of the analogue signals in the digital domain. A predefined number of samples are collected and are then analyzed block-wise, with the optimal sampling period depending on the dynamics of the system (phase drift) and noise characteristics (lock-in time constant).

For the current system, a decimation period of 1 s was found to be optimal. In the first step, the DC signals $I_{k,s}$ are averaged over the decimation period

$$I_k = \frac{1}{S}\sum_{s=1}^{S} I_{k,s}, \tag{5}$$

where the subscript s denotes the sample index of the high-resolution data (50 kHz), and S the total number of samples in the sampling period ($S = 50{,}000$ in the presented experiments). In a second step, the high-resolution AC signals are filtered for common-mode noise. For a 2×2 coupler, the normalization with total intensity in Eq. (4) suppresses common-mode noise arising from, e.g., small fluctuations in probe laser intensity. A similar correction needs to be implemented in the 3×3 coupler algorithms because common-mode noise, even if in the sub-per-mille range, will affect the calculated final product and will compromise the measurement accuracy. From the time-averaged DC signals I_k, the total output intensity I_{tot} is calculated:

$$I_{\text{tot}} = \sum_{k=1}^{3} I_k. \tag{6}$$

The sum of the high-resolution AC signals is used to increase the precision of the measured intensity, as the absolute values of the DC signals are limited by the 16-bit quantization of the DAQ:

$$I^*_{\text{tot},s} = I_{\text{tot}} + \sum_{k=1}^{3} i_{k,s}. \tag{7}$$

The three AC signals can be corrected for transient small changes in laser intensity, according to

$$i^*_{k,s} = i_{k,s} - \left(\frac{I^*_{\text{tot},s}}{I_{\text{tot}}} - 1\right) I_k, \tag{8}$$

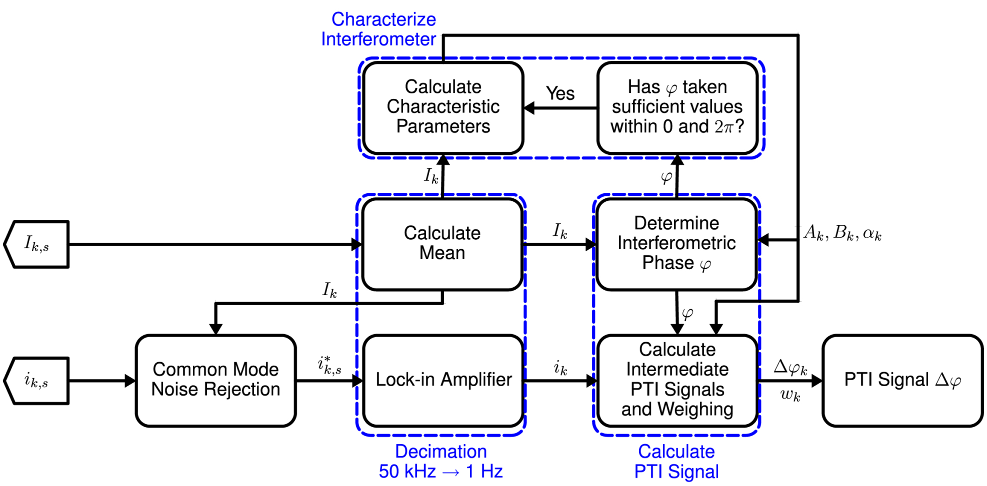

Fig. 5. Signal flow diagram for the retrieval of the interferometric phase φ and the PTI signal $\Delta\varphi$. Three lock-in amplifiers are used to calculate intermediate PTI signals $\Delta\varphi_k$, which are then weighted to obtain $\Delta\varphi$.

where the term in brackets describes the rapid relative change of the measured total light intensity. By multiplication with the actual intensity I_k, the signal contribution caused by common-mode noise is calculated and subtracted from the measured AC signal $i_{k,s}$. Using Eq. (7), this simplifies to

$$i^*_{k,s} = i_{k,s} - \frac{\sum_{k=1}^{3} i_{k,s}}{I_{\text{tot}}} I_k, \tag{9}$$

where $i^*_{k,s}$ are the common mode noise filtered AC signals.

These signals are then passed to three individual lock-in algorithms. The signals are demodulated, and information on the PTI-induced phase change is extracted from the AC signals using the known carrier from the excitation. Sine and cosine demodulation is performed simultaneously (dual-phase demodulation). From the lock-in algorithms, the amplitude R_k and phase θ_k of the AC signals are obtained at the modulation frequency. For an ideal system, θ_k is expected to be the same for all three outputs, i.e., it represents the response of the interferometer to the modulation of the pump laser. These response phases are denoted as θ^*_k. They are device-specific, and these phases are given, for example, by time delays from the laser driver and AC filters. They must be experimentally determined for proper demodulation [see Supplement 1 for more information].

As a result, the demodulated signals are

$$i_k = R_k \cos\left(\theta_k - \theta^*_k\right). \tag{10}$$

The sign of i_k depends on the slope of the detector signal (see Fig. 4) and is expressed in a change of θ_k, i.e., a phase shift of 180° is observed in θ_k with a change in sign of the detector slope.

As the interferometer is not held in phase quadrature, the phase-dependent sensitivity of the PTI response must be characterized and corrected. The characteristics of the interferometer (contrast and phase of each output) can be determined by performing, e.g., a phase scan over multiple cycles, which can be realized by gradually changing the pressure in the reference cell. During such a characterization procedure, the DC signals are recorded, and the amplitude A_k and offset B_k of each detector signal are determined.

In a symmetric 3×3 coupler, each of the three outputs has an intrinsic phase difference of 120° with respect to both other outputs. Moreover, the amplitude and offset would be identical for each detector. However, in a real, non-symmetric 3×3 coupler, this phase relation of the outputs does not necessarily hold, as well the equality of amplitudes and offsets. Hence, the actual phases of the output signals, referred to as the output phases (α_k), must be determined to allow phase-dependent correction of the calculated signal. For simplicity, α_1 is arbitrarily set to 0, i.e., I_1 is maximum at the interferometer phase $\varphi = 0$.

For an asymmetric (general) coupler, the equations for the kth detector can be written as

$$I_k = A_k \cos(\varphi - \alpha_k) + B_k. \tag{11}$$

There are a number of ways of determining A_k, B_k, and α_k from the experimental data. We developed a robust method that does not rely on actively controlled phase scans. It utilizes the data from a standard measurement by recording the random passage over a sufficient number of phases. With knowledge of the output phases α_k, the current phase of the interferometer φ can then be reconstructed from the DC signals I_k (see Supplement 1 for more information). The phase φ is used in the further computational steps in which the PTI signals $\Delta\varphi$ are reconstructed. As these signals are comparatively small ($\Delta\varphi$ is in the microrad range), they cannot be resolved in the DC-coupled signals and must be derived from the amplified and demodulated AC components.

In the following, we introduce $\Delta\varphi_k$, which represents the reconstructed PTI signal from the kth channel and will be denoted as an intermediate PTI signal. The demodulated AC signals (i_k) are related to the DC signals and intermediate PTI signals with the following linearization:

$$i_k = \frac{\mathrm{d}I_k}{\mathrm{d}\varphi} \Delta\varphi_k. \tag{12}$$

By definition, the demodulated signals are related to the PTI-induced phase change $\Delta\varphi_k$ as follows:

$$i_k = \frac{\mathrm{d}I_k}{\mathrm{d}\varphi} \Delta\varphi_k = \frac{\mathrm{d}}{\mathrm{d}\varphi} \left(A_k \cos(\varphi - \alpha_k) + B_k\right) \Delta\varphi_k \tag{13}$$

$$= -A_k \sin(\varphi - \alpha_k) \Delta\varphi_k. \tag{14}$$

This can be rearranged in terms of $\Delta\varphi_k$:

$$\Delta\varphi_k = -\frac{i_k}{A_k \sin(\varphi - \alpha_k)}. \tag{15}$$

As mentioned before, $\Delta\varphi_k$ is a purely mathematical construct representing the phase change determined by the kth channel, as there is only one modulated phase shift $\Delta\varphi$ resulting from the PTI measurement. To identify $\Delta\varphi$, it has to be considered that the sensitivity (and thus the noise) of the outputs is strongly phase dependent. Therefore, the three outputs are weighted with weighing factors w_k based on the sensitivity at the current phase, i.e., the absolute value of the slope of the response curve $\frac{\mathrm{d}I_k}{\mathrm{d}\varphi}$:

$$w_k = A_k |\sin(\varphi - \alpha_k)|. \tag{16}$$

As a final product, the PTI-induced phase shift is then the weighted arithmetic mean of the phase shifts determined from the three individual outputs:

$$\Delta\varphi = \frac{\sum_{k=1}^{3} w_k \Delta\varphi_k}{\sum_{k=1}^{3} w_k}. \tag{17}$$

The numerator of Eq. (17) therefore becomes

$$\sum_{k=1}^{3} w_k \Delta\varphi_k = -\sum_{k=1}^{3} i_k \frac{|\sin(\varphi - \alpha_k)|}{\sin(\varphi - \alpha_k)}, \tag{18}$$

which is simply the sum of the demodulated signals multiplied by the sign of their derivatives at the current interferometer phase. The sine terms can then be replaced with a logical test for the calculation. The denominator of Eq. (17) is

$$\sum_{k=1}^{3} w_k = \sum_{k=1}^{3} A_k |\sin(\varphi - \alpha_k)|. \tag{19}$$

This term represents the overall phase-dependent sensitivity of the measurement.

5. EXPERIMENTAL VALIDATION

A. Calibration with a Gas of Known Absorption

For calibration of the setup, a defined concentration of light absorbing gas (10 ppm NO_2 in synthetic air) was provided by [38] in a pressure cylinder. The mixing ratio was verified at the factory using the chemiluminescence method (uncertainty of ±3%). The cylinder was connected to a gas manifold, where either filtered clean air or the gas containing NO_2 was fed into the measuring chamber of the MiniPTI at a flow rate of 0.2 L/min. Teflon hoses were used to avoid absorption losses in the supply lines.

Measurements were performed with PTI setups using the fused fiber and the MMI coupler. Figure 6 shows the temporal evolution of the measured DC signals (I_k, 1 s resolution), the derived interferometric phase (φ, 1 s), and the retrieved PTI signal ($\Delta\varphi$, 1 and 60 s running average).

During the course of these experiments, the reference chamber was filled with clean air. The measurement chamber was initially flooded with filtered compressed air, then with a defined mixture of NO_2 in synthetic air, and this cycle was repeated 3 times. The influence of the injection of 10 ppm NO_2 resulted in a distinct increase of $\Delta\varphi$.

In these experiments, the interferometric phase φ drifted freely (no active quadrature control), demonstrating the phase independence of the PTI measurement. The observed continuous drift in φ is attributed to small temperature or pressure changes in the system. Another possible cause is a drift of the probe laser frequency.

From these experiments, the coupler-specific parameters, i.e., the amplitudes A_k, offsets B_k, and the output phases α_k were determined using the procedures described in Supplement 1 and are listed in Table 1. Furthermore, the system characteristic phases (response phases) θ_k^* are given. The fused-fiber coupler is very close to the ideal case: it has uniformly high contrast, and the phase differences are close to 120°. The MMI coupler, on the other hand, shows significantly larger asymmetries, both in the amplitudes and in the output phases. The table also shows that different probe lasers and load resistors were used in these two experiments.

NO_2 is a strongly absorbing gas, and a known concentration of NO_2 can be used to calibrate the PTI response of the MiniPTI. Using absorption data from Vandaele *et al.* [39], 10 ppm of NO_2 has an absorption coefficient of $b_{abs} = 11\,500 \pm 100\ \mathrm{Mm}^{-1}$ for the current experimental conditions at the 450 nm pump laser wavelength. The indicated error in b_{abs} is given by the relatively wide excitation laser spectrum of several nanometers (nm). It was estimated by a convolution of this bandwidth and the wavelength-dependent NO_2 molecular absorption cross section.

Knowing b_{abs} of 10 ppm NO_2, the calibration factor C [see Eq. (3)] was determined for the two presented experiments (see Table 2). A good agreement in the C-values is expected, as the sensitivity of the PTI system is mainly determined by the geometry of the pump and probe laser overlap and the excitation strength (pump laser power). However, we observed a

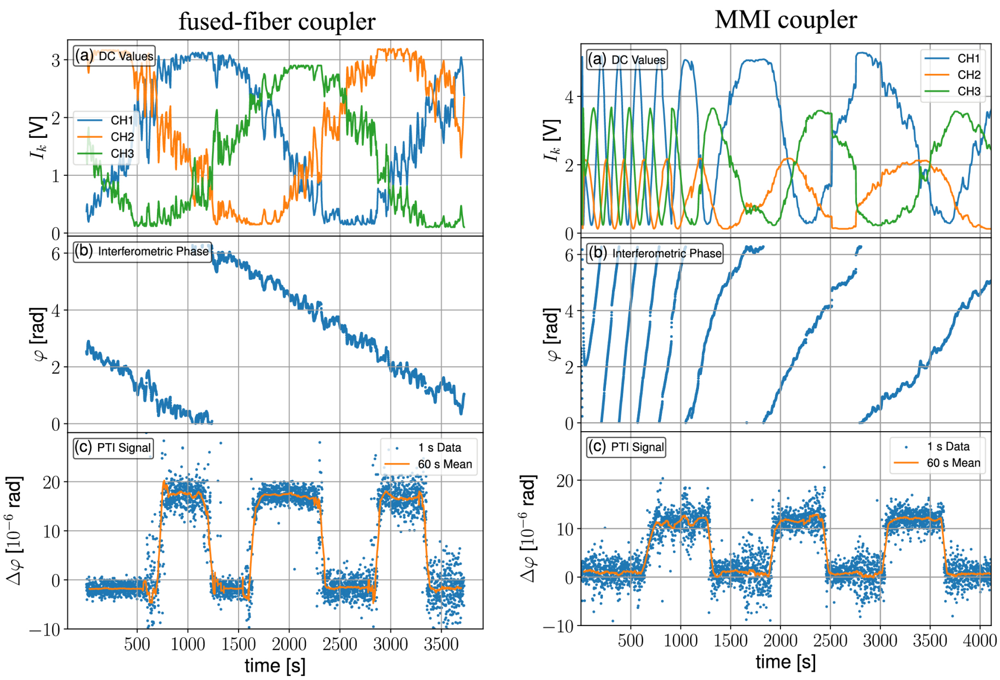

Fig. 6. Typical calibration measurement cycle for the setup using the fused-fiber coupler (left) and the MMI coupler (right) as the recombining 3 × 3 coupler. (a) Time evolution of the measured DC signals and (b) the derived interferometric phase. While performing these experiments, clean air and air with absorbing gas (10 ppm NO_2) were alternately introduced into the measurement chamber, resulting in a distinct increase of the PTI signals $\Delta\varphi$ (c). Note that the detected changes in $\Delta\varphi$ are in the microradian (μ-rad) range.

Table 1. Characteristic Values of the Two Couplers Derived by the Inversion Algorithm at the Beginning of the Measurements (see Supplement 1 for More Information)[a]

Channel k	A_k [V]	B_k [V]	α_k [deg]	θ_k^* [deg]
(a) Fused-Fiber Coupler				
1	1.49	1.63	0	130 ± 4
2	1.51	1.66	123.3	132 ± 3
3	1.39	1.51	242.5	138 ± 7
(b) MMI Coupler				
1	2.44	2.71	0.00	110 ± 28
2	1.07	1.14	105.8	123 ± 29
3	1.70	1.94	215.3	120 ± 9

[a]When interpreting the amplitudes A_k and offsets B_k, it must be taken into account that different series resistors and probe lasers were used: (a) $R_L = 820\Omega$, $P_{\text{Probelaser}} = 20$ mW (DK Photonics); (b) $R_L = 34\text{k}\Omega$, $P_{\text{Probelaser}} = 2$ mW (Thorlabs). The standard deviation of θ_k^* is also specified. The uncertainty for A_k, B_k, α_k by the retrieval is found to be small (<0.1%) and is not given here.

Table 2. Calibration Values and PTI Noise for the Measurements Shown in Fig. 6[a]

Coupler	Calibration Factor C $[10^8 \frac{1}{\text{Mm}} \frac{1}{\text{rad}}]$	Noise in $\Delta\varphi$ $(1\sigma, 1\text{ s})$ $[10^{-6}$ rad]	Noise in $\Delta\varphi$ $(1\sigma, 60\text{ s})$ $[10^{-6}$ rad]
Fused-Fiber	6.17	1.96	0.21
MMI	10.50	2.25	0.29

[a]The instrumental noise is represented as standard deviation σ, which was calculated for constant experimental conditions for 1 and 60 s aggregated data.

42% lower sensitivity for the MMI experiment, expressed in a higher C-value. This deviation cannot be attributed to the use of different 3×3 couplers and two different probe lasers. It is partly explained by an observed 12% decrease in the pump laser intensity during the MMI experiment. In addition, a slight misalignment of the pump laser in the MMI experiment cannot be excluded.

It is noteworthy in Fig. 6 that the noise in the 1 s DC signals (and also in the interferometric phase) is much larger in the experiment with the fused-fiber coupler than with the MMI. We suspect that this low-frequency noise is caused by different phase noise of the lasers used in the two setups (see Table 1). However, this noise component does not manifest itself equally in the PTI signal, i.e., at the pump laser modulation frequency of 80 Hz. The presented experiments show that both setups can measure stable PTI signals ($\Delta\varphi$) in the microrad range.

A long-term experiment (65 h) was performed to determine the instrumental noise dependence on the integration time and the analysis (modified Allan plot) can be found in the SI. In the following, we restrict ourselves to the standard deviation of $\Delta\varphi$ for the 1 and 60 s data determined for background conditions (see Table 2). The C-value can be used to convert this noise into an instrumental detection limit for the absorption coefficient (with an average over 60 s). This translates into a 1σ detection limit of $b_{\text{abs}} = 126\ \text{Mm}^{-1}$ and $305\ \text{Mm}^{-1}$, for the fused-fiber and MMI setup, respectively. Assuming a BC mass absorption cross section (MAC) of $10\ \text{m}^2/\text{g}$, this corresponds to BC detection limit of the MiniPTI in the order of $10\ \mu\text{g/m}^3$ $(1\sigma, 60$ s average).

As mentioned earlier, the phase is not controlled in these experiments and varies freely. Figure 6 shows that the retrieved PTI signals are not fading even with the MMI, which has a comparatively pronounced asymmetry. However, this asymmetry is responsible for the phase-dependent magnitude of the noise in the PTI signal (seen in the MMI experiment at, e.g., $t = 1100$, 1700, 2800 s). The signal contribution of the three channels to the PTI signal is considered in the algorithm by including the respective slopes $(-A_k \sin(\varphi - \alpha_k))$. AC noise, on the other hand, is amplified accordingly by this method for channels with a small slope caused by the low amplitude (CH2 in this example).

B. Concentration Series with Absorbing Aerosols

Further experiments with the fused-fiber coupler were performed during a measurement campaign with aerosolized nigrosin, a black dye [16]. Here a nebulizer was filled with a set of dilute solutions of nigrosin to produce varying concentrations and size distributions of nigrosin aerosol. The generated droplets were subsequently dried using a diffusion drier and further diluted with dry compressed air using a rotating disc diluter. The diluted aerosol was filled into a buffer volume designed to damp pressure variations caused by the rotating disc diluter and subsequently sampled by a number of *in situ* and *ex situ* aerosol light absorption instruments including the MiniPTI, a free-space PTI (MSPTI [17]) operating at 532 nm, a custom-built photoacoustic instrument, and a filter-based absorption instrument (AE33 Aethalometer). The concentration of the nigrosin aerosol was monitored using a light scattering sensor, and the size distribution of the aerosol particles with a scanning mobility particle sizer (SMPS). In order to test the response of the MiniPTI to light absorption by nigrosin aerosol, the measured signals were transferred to absorption coefficients via the NO_2 calibration and compared to the light absorption measured by the MSPTI. Both instruments were attached to the same sampling line and recorded the same measurement cycle: 800 s aerosol sampling followed by 300 s of background (filtered aerosol). Each 800 s sampling period was averaged, and the background subtracted. A comparison of the MiniPTI and MSPTI absorption measurements is shown in Fig. 7, whereby the error bars denote 1σ of the 60 s averaged data during the measurement period. Data points with significant error bars for the MSPTI measurements denote measurement periods during which the aerosol concentration was changing. The overall noise in both interferometer signals was higher than for standard laboratory measurements due to the number of instruments with pumps sharing a single sampling line.

The data in Fig. 7 was fitted with a linear function

$$b_{\text{abs,MiniPTI}} = (-92 \pm 29)\text{Mm}^{-1} + (0.65 \pm 0.01) b_{\text{abs,MSPTI}} \quad \textbf{(20)}$$

and the coefficient of determination of $R^2 = 0.98$ shows the linear relationship between the measured absorption coefficients of the two instruments. The slope of 0.65 between the MiniPTI (450 nm) and the MSPTI (532 nm) is primarily due to the absorption spectrum of nigrosin, which peaks in the visible region at around 580 nm. Interpolation of the nigrosin spectra from the literature leads to absorption ratios of 0.68 [40] to 0.75 [16]. A UV-VIS measurement of a nigrosin solution performed

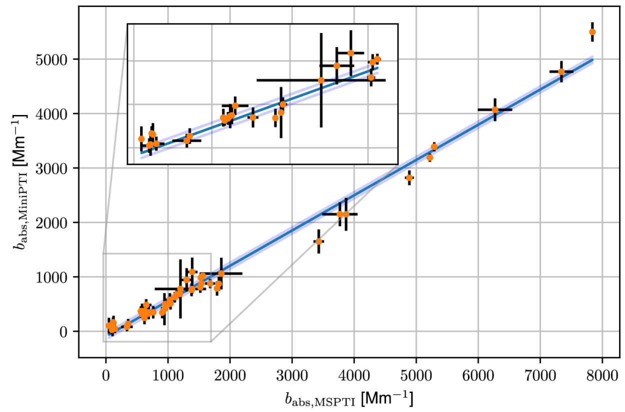

Fig. 7. Comparison of the absorption coefficients for nigrosin aerosol measured with the MiniPTI and the MSPTI (reference instrument). The data points represent the average over one measurement cycle (800 s; see body text for further details), with the error bars representing 1σ of the 60 s averaged data during the measurement period. The linear regression and the 95% prediction interval are shown in blue and light blue, respectively.

in house gave an absorption ratio of 0.78. Hence, the slope of the linear regression of the PTI absorption data is in good agreement with the absorption ratio calculated from the data of Bluvshtein *et al*. [40]. The sources of uncertainty in the measurements are primarily the transfer of the absorption spectrum of nigrosin from solution to the gas phase, the uncertainty in the NO_2 calibration of the MiniPTI ($\approx 10\%$) due to the uncertainty in the emission spectrum of the laser, and the lack of highly resolved spectral data for nigrosin (the spectral bandwidth of the Nd:YAG laser in the MSPTI is much smaller than the resolution of the literature spectra, though the spectra are expected to be smooth).

6. NOISE ANALYSIS

A set of experiments were performed to quantify the noise sources for the current MiniPTI setup, in which components of the setup were progressively disabled. From these experiments, it was determined that the primary noise component ($\approx 98\%$) was interferometer phase noise arising from differential changes in the optical path lengths of the measurement and reference arms of the interferometer at the measurement frequency. This noise is primarily ascribed to vibrations of the fibers, GRIN lenses, and holders changing the physical path length of the interferometer arms and, to a lesser degree, turbulence (local pressure variations) in the measurement chamber. Phase noise additionally arises indirectly from frequency noise in the probe laser, as the measurement and reference path lengths are not exactly equal. There was also evidence of a photoacoustic signal, caused by the absorption of the pump laser light by the window between the measurement and reference chambers, though this was primarily observed as a baseline offset, rather than adding to the noise. Laser intensity noise was found to be only a small component of the overall noise ($\approx 2\%$), while electronic and acquisition noise were determined to be inconsequential for the current setup. The signal amplitude and thus the SNR could be improved by increasing the power of the pump laser (linear relationship), though the goal of a miniature instrument places a cap on any significant increases in laser power. Instead, a considerable advantage could be gained by reducing the phase noise in the system. This could be achieved by changing the interferometer geometry to a folded one (see, e.g., [13]) and mounting the GRIN lenses on a single plate to reduce the influence of vibration. Another considerable improvement could be achieved by replacing the fiber optic components with a custom-made waveguide. In this way the arm lengths of the interferometer would be considerably reduced, making it also easier to equalize them. This change has the advantage of reducing the susceptibility of the MiniPTI to external noise sources such as vibration but also has the potential to significantly reduce the probe laser frequency component of the phase noise. The frequency noise component could also be addressed directly through the purchase of a stabilized probe laser with narrower spectral bandwidth.

7. CONCLUSION

We have developed a new inversion scheme to demodulate the phase signal of a waveguide-based photothermal interferometer for measuring light absorption. Experiments with 3×3 couplers of different working principles as beam recombination optics demonstrate the passive operation of the system. The retrieved PTI signal amplitude does not depend on the actual interferometric phase. No quadrature point control is needed, which significantly reduces the hardware requirements of the system. The algorithm, which works for imperfect asymmetric couplers, is tested with 10 ppm NO_2 and varying concentrations of light-absorbing carbonaceous aerosols. The PTI signal noise is about 0.2 microrad (1σ, 60 s), corresponding to an optical path change of about 40 femtometers. This noise defines the current instrumental detection limit, which is above 100 Mm^{-1} in terms of light absorption coefficient, or about 10 $\mu g/m^3$ in BC mass concentration. Analysis shows that the primary noise component is phase noise of the interferometer, caused by, e.g., frequency noise in the probe laser or vibrations of optical components such as the fibers.

The setup offers massive room for improvement: It has the potential to be miniaturized, as a future interferometer can be built on a centimeter-sized chip. Reducing the optical path length (currently ≈ 70 cm) and using stiffer integrated components (increased stability by eliminating vibration-prone free-space elements) will further increase sensitivity and significantly reduce cost. Such miniaturization steps are currently underway, and we are working on a PIC-based photothermal interferometer design that eliminates the optical fibers in the arms between the two couplers.

Funding. H2020 Research and Innovation Programme (101016956, PASSEPARTOUT Project) in the context of the Photonics Public Private Partnership; Innosuisse–Swiss Innovation Agency (42794.1 IP-EE).

Acknowledgment. We thank Patrick Specht for his assistance and technical expertise and Luka Drinovec, Griša Močnik, Martin Wiederkehr, Miklós Lenner, Daniel Schindler for fruitful discussions. Valentin Strässle, Markus Halter, and Thomas Hughes are acknowledged for their innovative development work in the manufacturing of planar waveguides. We thank

Samuel Häusler for careful reading of the manuscript and for the fruitful and constructive exchange.

Disclosures. The authors declare no conflicts of interest.

Data availability. The data presented in this paper are available together with the implementation of the presented algorithm (retrieval of interferometric phase and characteristic parameters) in our GitHub repository [41].

Supplemental document. See Supplement 1 for supporting content.

REFERENCES

1. European Environment Agency (EEA), Air Quality in Europe 2021 (2021).
2. N. A. H. Janssen, G. Hoek, M. Simic-Lawson, P. Fischer, L. van Bree, H. ten Brink, M. Keuken, R. W. Atkinson, H. R. Anderson, B. Brunekreef, and F. R. Cassee, "Black carbon as an additional indicator of the adverse health effects of airborne particles compared with PM10 and PM2.5," Environ. Health Perspect. **119**, 1691–1699 (2011).
3. T. C. Bond, S. J. Doherty, D. W. Fahey, *et al.*, "Bounding the role of black carbon in the climate system: a scientific assessment," J. Geophys. Res. Atmos. **118**, 5380–5552 (2013).
4. V. Masson-Delmotte, P. Zhai, A. Pirani, C. P. S. L. Connors, S. Berger, N. Caud, Y. Chen, L. Goldfarb, M. Gomis, M. Huang, K. Leitzell, E. Lonnoy, J. Matthews, T. Maycock, T. Waterfield, O. Yelekçi, R. Yu, and B. Zhou, eds., "Climate Change 2021: The physical science basis," in *Contribution of Working Group I to the Sixth Assessment Report of the Intergovernmental Panel on Climate Change (IPCC)* (Cambridge University, 2021).
5. H. Moosmüller, R. Chakrabarty, and W. Arnott, "Aerosol light absorption and its measurement: a review," J. Quant. Spectrosc. Radiat. Transf. **110**, 844–878 (2009).
6. C. C. Davis and S. J. Petuchowski, "Phase fluctuation optical heterodyne spectroscopy of gases," Appl. Opt. **20**, 2539–2554 (1981).
7. S. F. Fulghum and M. M. Tilleman, "Interferometric calorimeter for the measurement of water-vapor absorption," J. Opt. Soc. Am. B **8**, 2401–2413 (1991).
8. D. L. Mazzoni and C. C. Davis, "Trace detection of hydrazines by optical homodyne interferometry," Appl. Opt. **30**, 756–764 (1991).
9. D. M. Kalbermatter, G. Močnik, L. Drinovec, B. Visser, J. Röhrbein, M. Oscity, E. Weingartner, A.-P. Hyvarinen, and K. Vasilatou, "Comparing black carbon and aerosol absorption measuring instruments–a new system using lab-generated soot coated with controlled amounts of secondary organic matter," Atmos. Meas. Tech. **15**, 561–572 (2022).
10. D. U. Fluckiger, H.-B. Lin, and W. H. Marlow, "Composition measurement of aerosols of submicrometer particles by phase fluctuation absorption spectroscopy," Appl. Opt. **24**, 1668–1681 (1985).
11. D. Lack, H. Moosmüller, G. McMeeking, R. Chakrabarty, and D. Baumgardner, "Characterizing elemental, equivalent black, and refractory black carbon aerosol particles: a review of techniques, their limitations and uncertainties," Anal. Bioanal. Chem. **406**, 99–122 (2014).
12. H.-B. Lin and A. J. Campillo, "Photothermal aerosol absorption spectroscopy," Appl. Opt. **24**, 422–433 (1985).
13. H. Moosmüller and W. Arnott, "Folded Jamin interferometer: a stable instrument for refractive-index measurements," Opt. Lett. **21**, 438–440 (1996).
14. A. J. Sedlacek and J. Lee, "Photothermal interferometric aerosol absorption spectrometry," Aerosol Sci. Technol. **41**, 1089–1101 (2007).
15. A. J. Sedlacek, "Real-time detection of ambient aerosols using photothermal interferometry: folded Jamin interferometer," Rev. Sci. Instrum. **77**, 064903 (2006).
16. L. Drinovec, U. Jagodič, L. Pirker, M. Škarabot, M. Kurtjak, K. Vidović, L. Ferrero, B. Visser, J. Röhrbein, E. Weingartner, D. M. Kalbermatter, K. Vasilatou, T. Bühlmann, C. Pascale, T. Müller, A. Wiedensohler, and G. Močnik, "A dual-wavelength photothermal aerosol absorption monitor: design, calibration and performance," Atmos. Meas. Tech. **15**, 3805–3825 (2022).
17. B. Visser, J. Röhrbein, P. Steigmeier, L. Drinovec, G. Močnik, and E. Weingartner, "A single-beam photothermal interferometer for in situ measurements of aerosol light absorption," Atmos. Meas. Tech. **13**, 7097–7111 (2020).
18. W. Jin, Y. Cao, F. Yang, and H. L. Ho, "Ultra-sensitive all-fibre photothermal spectroscopy with large dynamic range," Nat. Commun. **6**, 6767 (2015).
19. S. K. Sheem, T. G. Giallorenzi, and K. Koo, "Optical techniques to solve the signal fading problem in fiber interferometers," Appl. Opt. **21**, 689–693 (1982).
20. K. P. Koo, A. B. Tveten, and A. Dandridge, "Passive stabilization scheme for fiber interferometers using (3×3) fiber directional couplers," Appl. Phys. Lett. **41**, 616–618 (1982).
21. R. Priest, "Analysis of fiber interferometer utilizing 3 × 3 fiber coupler," IEEE J. Quantum Electron. **18**, 1601–1603 (1982).
22. O. T. Kamenev, Y. S. Petrov, and A. A. Podlesnykh, "Use of 3×3 coupler in the fiber optic strainmeter based on Mach-Zehnder interferometer," KnE Energy **3**, 388–392 (2018).
23. D. Brown, C. Cameron, R. Keolian, D. Gardner, and S. Garrett, "A symmetric 3×3 coupler based demodulator for fiber optic interferometric sensors," Proc. SPIE **1584**, 328 (1991).
24. Y. Wu, H. Tang, and C. Wang, "Study on the performance of passive digital phase demodulation algorithm based on 3×3 coupler and the hardware implementation," Proc. SPIE **11607**, 49–58 (2021).
25. B. Chiu and M. C. Hastings, "Digital demodulation for passive homodyne optical fiber interferometry based on a 3 by 3 coupler," Proc. SPIE **2292**, 371–382 (1994).
26. Y. Fei, X. Dan, C. Haiwen, and Q. Ronghui, "120° phase difference interference technology based on 3 × 3 coupler and its application in laser noise measurement," in *Optical Interferometry*, A. A. Banishev, M. Bhowmick, and J. Wang, eds. (IntechOpen, 2017), chap. 11.
27. O. T. Kamenev, Y. S. Petrov, A. A. Podlesnykh, V. A. Kolchinskii, I. N. Zavestovskaya, Y. N. Kulchin, and R. V. Romashko, "Recording of hydroacoustic signals using a fiber-optic accelerometer," Bull. Lebedev Phys. Inst. **47**, 146–148 (2020).
28. S.-C. Her and C.-M. Yang, "Dynamic strain measured by Mach-Zehnder interferometric optical fiber sensors," Sensors **12**, 3314–3326 (2012).
29. L. K. Cheng, R. A. J. Hagen, L. N. Schriek, P. M. Toet, and O. van der Togt, "Fiber interferometer combining sub-nm displacement resolution with miniaturized sensor head," in *Proc. Volume 10323, 25th International Conference on Optical Fiber Sensors* (SPIE2017), p. 1032380.
30. R. J. J. van Gulik, B. M. de Boer, and P. J. Harmsma, "Refractive index sensing using a three-port interferometer and comparison with ring resonators," IEEE J. Sel. Top. Quantum Electron. **23**, 433–439 (2017).
31. M. D. J. Todd, G. A. Johnson, and B. L. Althouse, "A novel Bragg grating sensor interrogation system utilizing a scanning filter, a Mach-Zehnder interferometer and a 3 x 3 coupler," Meas. Sci. Technol. **12**, 771–777 (2001).
32. S.-T. Shih, M.-H. Chen, and W. W. Lin, "Analysis of distortion of a fiber optic Michelson interferometric sensor caused by the imperfect properties of its 3x3 coupler," Opt. Eng. **36**, 2101–2106 (1997).
33. Z. Zhao, M. Demokan, and M. MacAlpine, "Improved demodulation scheme for fiber optic interferometers using an asymmetric 3 × 3 coupler," J. Lightwave Technol. **15**, 2059–2068 (1997).
34. E. Kleijn, E. M. van Vliet, D. Pustakhod, M. K. Smit, and X. L. M. Leijtens, "Amplitude and Phase Error Correction Algorithm for 3 x 3 MMI Based Mach-Zehnder Interferometers," J. Lightwave Technol. **33**, 2233–2239 (2015).
35. "FS", https://www.fs.com.
36. "vario-optics AG", https://vario-optics.ch/.
37. J. Kremmel, N. Crameri, T. Lamprecht, and M. Michler, "Passive aligned assembly of an integrated optical displacement sensor based on a reflective Mach–Zehnder interferometer with a 3 × 3 directional coupler," Opt. Eng. **57**, 087103 (2018).

38. “Messer Schweiz AG”, https://www.messer.ch/.
39. A. C. Vandaele, C. Hermans, S. Fally, M. Carleer, R. Colin, M.-F. Mérienne, A. Jenouvrier, and B. Coquart, “High-resolution Fourier transform measurement of the NO_2 visible and near-infrared absorption cross sections: temperature and pressure effects,” J. Geophys. Res. Atmos. **107**, ACH 3–1 (2002).
40. N. Bluvshtein, J. M. Flores, Q. He, E. Segre, L. Segev, N. Hong, A. Donohue, J. N. Hilfiker, and Y. Rudich, “Calibration of a multi-pass photoacoustic spectrometer cell using light-absorbing aerosols,” Atmos. Meas. Tech. **10**, 1203–1213 (2017).
41. J. Bilal, “MiniPTI,” GitHub (2020) [accessed 3 January 2023], https://github.com/bilaljo/MiniPTI.